SEPIA345: A 345 GHz dual polarization heterodyne receiver channel for SEPIA at the APEX telescope

Citation for the original published paper (version of record):

Meledin, D., Lapkin, I., Fredrixon, M. et al (2022). SEPIA345: A 345 GHz dual polarization
heterodyne receiver channel for SEPIA at the APEX
telescope. Astronomy and Astrophysics, 668. http://dx.doi.org/10.1051/0004-6361/202244211

(article starts on next page)

Astronomy & Astrophysics

SEPIA345: A 345 GHz dual polarization heterodyne receiver channel for SEPIA at the APEX telescope

D. Meledin[1,2], I. Lapkin[1,2], M. Fredrixon[1,2], E. Sundin[1,2], S.-E. Ferm[1,2], A. Pavolotsky[1,2], M. Strandberg[1,2],
V. Desmaris[1], C. López[1], P. Bergman[2], M. Olberg[2], J. Conway[2], K. Torstensson[4,5], C. Durán[4],
F. M. Montenegro-Montes[4,6,7], C. De Breuck[3], and V. Belitsky[1]

[1] Group for Advanced Receiver Development (GARD), Department of Space, Earth and Environment, Chalmers University of Technology, 41296 Gothenburg, Sweden
e-mail: denis.meledin@chalmers.se
[2] Department of Space, Earth and Environment, Chalmers University of Technology, Onsala Space Observatory (OSO), 43992 Onsala, Sweden
[3] European Southern Observatory (ESO), Karl-Schwarzschild-Str. 2, 85748 Garching bei München, Germany
[4] European Southern Observatory, Alonso de Córdova 3107, Vitacura, Casilla 19001, Santiago de Chile, Chile
[5] Joint ALMA Observatory, Alonso de Córdova 3107, Vitacura 763-0355, Santiago de Chile, Chile
[6] Departamento de Física de la Tierra y Astrofísica, Universidad Complutense de Madrid, 28040 Madrid, Spain
[7] Instituto de Física de Partículas y del Cosmos IPARCOS, Fac. de Ciencias Físicas, Univ. Complutense de Madrid, 28040 Madrid, Spain

Received 7 June 2022 / Accepted 17 September 2022

ABSTRACT

Context. We describe the new SEPIA345 heterodyne receiver channel installed at the Atacama Pathfinder EXperiment (APEX) telescope, including details of its configuration, characteristics, and test results on sky. SEPIA345 is designed and built to be a part of the Swedish ESO PI Instrument for the APEX telescope (SEPIA). This new receiver channel is suitable for very high-resolution spectroscopy and covers the frequency range 272–376 GHz. It utilizes a dual polarization sideband separating (2SB) receiver architecture, employing superconductor-isolator-superconductor mixers (SIS), and provides an intermediate frequency (IF) band of 4–12 GHz for each sideband and polarization, thus covering a total instantaneous IF bandwidth of $4 \times 8 = 32$ GHz.
Aims. This paper provides a description of the new receiver in terms of its hardware design, performance, and commissioning results.
Methods. The methods of design, construction, and testing of the new receiver are presented.
Results. The achieved receiver performance in terms of noise temperature, sideband rejection, stability, and other parameters are described.
Conclusions. SEPIA345 is a commissioned APEX facility instrument with state-of-the-art wideband IF performance. It has been available on the APEX telescope for science observations since July 2021.

Key words. instrumentation: detectors – techniques: spectroscopic – submillimeter: general

1. Introduction

For more than 15 yr, the Atacama Pathfinder EXperiment (APEX) telescope has exploited the excellent millimeter- and submillimeter-wavelength observing conditions above the Chajnantor plateau in northern Chile (Güsten et al. 2006). During this period the telescope has been operated as a collaboration between three partners: the Max Planck Institute for Radioastronomy (MPIfR), the European Southern Observatory (ESO), and Onsala Space Observatory (OSO). The APEX telescope is a modified 12-m diameter ALMA-prototype dish with a very high surface accuracy of 12–15 µm rms, making observations up to THz frequencies accessible (Wiedner et al. 2006; Meledin et al. 2009). Since the beginning of the project, the telescope has been equipped with a series of facility receivers that are available to the whole APEX scientific community. These have included the APEX-2A receiver (Risacher et al. 2006), LABOCA (Siringo et al. 2009) and the Swedish Heterodyne Facility Instrument (SHFI), (Vassilev et al. 2008).

The current complement of available APEX instruments include the facility nFLASH receiver[1] (Klein 2020), which consists of two independently tunable frequency channels: nFLASH230 and nFLASH460. Additionally, there are currently numerous PI instruments installed, including the bolometer camera ArTéMiS (Revéret et al. 2014; Hacar et al. 2013) and the LEKID detector camera CONCERTO (The CONCERTO Collaboration 2020).

A major component of the current set of APEX facility receivers is provided by the Swedish ESO PI Instrument for the APEX telescope (SEPIA), which is a multiband heterodyne instrument developed by the Group for Advanced Receiver Development (GARD) at Chalmers University of Technology and OSO, in collaboration with ESO (Belitsky et al. 2018b). This instrument features a cartridge layout that is fully compatible with ALMA technologies, enabling the installation and

---

[1] MPIfR, Sub-mm technology division, https://www.mpifr-bonn.mpg.de/5278273/nflash

usage of up to three ALMA compatible receiver cartridges. The SEPIA instrument therefore provides a reconfigurable platform for operating and testing different receivers.

The SEPIA instrument was installed at APEX in 2015 and was initially equipped only with the SEPIA180 receiver channel, a modified preproduction ALMA Band 5 cartridge (Belitsky et al. 2018a). Later, in 2016, SEPIA was augmented with the SEPIA660 receiver (ALMA Band 9 cartridge; Baryshev et al. 2015; Belitsky et al. 2018b) delivered by the Netherlands Research School for Astronomy (NOVA). This receiver channel was upgraded after 2 yr into a sideband separating (2SB) version with enhanced signal (RF) and intermediate frequency (IF) bands (Khudchenko et al. 2017; Hacar et al. 2020). Complementing the SEPIA receivers, MPIfR has provided the APEX telescope with a high-capacity fast-Fourier transform spectrometer (FFTS) backend, which can process as many as eight 4-GHz-wide sub-bands (Klein et al. 2012). The SEPIA receiver, together with this spectrometer, provides a state-of-the-art capability for high spectral resolution wide-band single-dish spectroscopic observations.

The construction and performance of the third SEPIA receiver channel, SEPIA345, is described in this paper. SEPIA345 operates over the frequency range 272–376 GHz. Many astrophysically important molecular transitions fall into this frequency range, for instance, ^{13}CO ($J = 3 \rightarrow 2$), CH_3OH ($J = 7 \rightarrow 6$), CO ($J = 3 \rightarrow 2$), CS ($J = 6 \rightarrow 5$), and HCN ($J = 4 \rightarrow 3$). The primary use of the SEPIA345 receiver is to observe these molecular transitions as part of the single-dish spectroscopic observing program of APEX.

In addition to its use for the above single-dish observations, the SEPIA345 receiver also expands APEX participation in Very Large Baseline Interferometry (VLBI) observations for the Event Horizon Telescope (EHT) from 230 GHz to 345 GHz. In April 2022 the SEPIA345 receiver channel was successfully involved in EHT test observations at 345 GHz. The scientific importance of EHT telescopes such as APEX moving to a higher observing frequency is that this gives longer VLBI baselines in terms of wavelengths, allowing higher-resolution images to be made of both the M87 (Event Horizon Telescope Collaboration 2019) and the Galactic Center black holes (Akiyama et al. 2022). For the latter target, there is the additional advantage at higher frequencies of reduced Galactic scattering, which again increases effective angular resolution.

In this paper, we present an overview of the SEPIA345 receiver channel and summarize the technical and science commissioning that took place from February 2020 to July 2021.

2. Receiver configuration

2.1. New SEPIA optical layout at facility position

Initially, when first installed in 2015, SEPIA occupied the visitor instrument position inside the A-Nasmyth cabin (Cabin A) at APEX. The corresponding initial optics arrangement and the layout of the SEPIA cryostat were described in Belitsky et al. (2018b). In 2019, the SEPIA instrument was moved to one of the facility instrument positions in Cabin A, where it now permanently resides (Lapkin et al. 2019). In this new position, the available space was limited due to the instrument support structure and the facility calibration unit (FCU). The implemented solution overcomes this complication and provides the optical path clearances required for all the instruments present in the cabin (Lapkin et al. 2019).
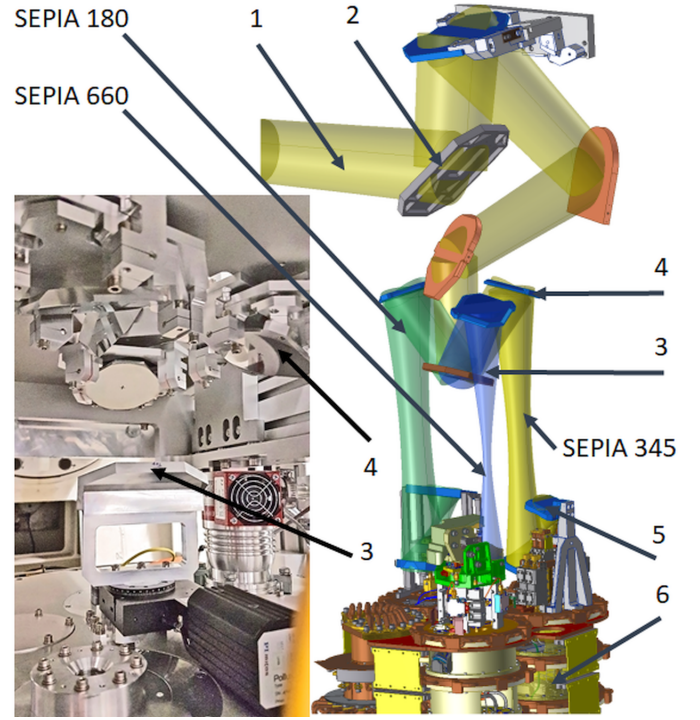
Fig. 1. Optical layout of SEPIA at its current facility instrument position. The following components are marked: 1 – the input beam coming from the antenna; 2 – the instrument selection mirror; 3 – the SEPIA band selection mirror; 4 – SEPIA345 band adjustable focusing mirror; 5 – SEPIA345 second cold mirror; 6 – SEPIA345 CCA.

The optical layout in SEPIA's current facility position is shown in Fig. 1. In the figure insert, a photo is shown of the available space between the top plate of the receiver and the focusing mirrors for the receiver channels. The focusing mirror for the SEPIA345 receiver band is marked as position 4 in Fig. 1. To be able to provide beam coupling in the limited cabin space, the SEPIA optics has as a total of ten mirrors, including five warm mirrors located before the instrument selection mirror (position 2, Fig. 1), which allows the choice between different astronomical instruments located in cabin A. Further along the optical path, there is a high-precision controlled cartridge selection mirror (position 3, Fig. 1) that selects which of the three SEPIA receiver channels has access to the sky. The optics design implements a frequency-independent illumination of the secondary for all receiver channels with an edge taper of about −12 dB (Lapkin et al. 2019). To be able to fulfill this condition within the entire SEPIA working frequency range (159–722 GHz), the complete optical path works as a reimaging system, transferring the image of the secondary reflector onto the aperture of the corrugated horn for each receiver channel.

As part of the receiver verification, measurements of the beam at several signal frequencies were performed in the lab as near-field scans over the cryostat window, close to the beam waist, at a distance of about 290 mm from the first cold mirror from the cryostat signal window. The calculated Gaussivity was found to be about 96%.

2.2. SEPIA345 receiver layout

The SEPIA345 receiver band covers 272–376 GHz and features a dual polarization 2SB layout. The RF signal (position 1, Fig. 1) propagates from the telescope main cabin (Cabin C) to the
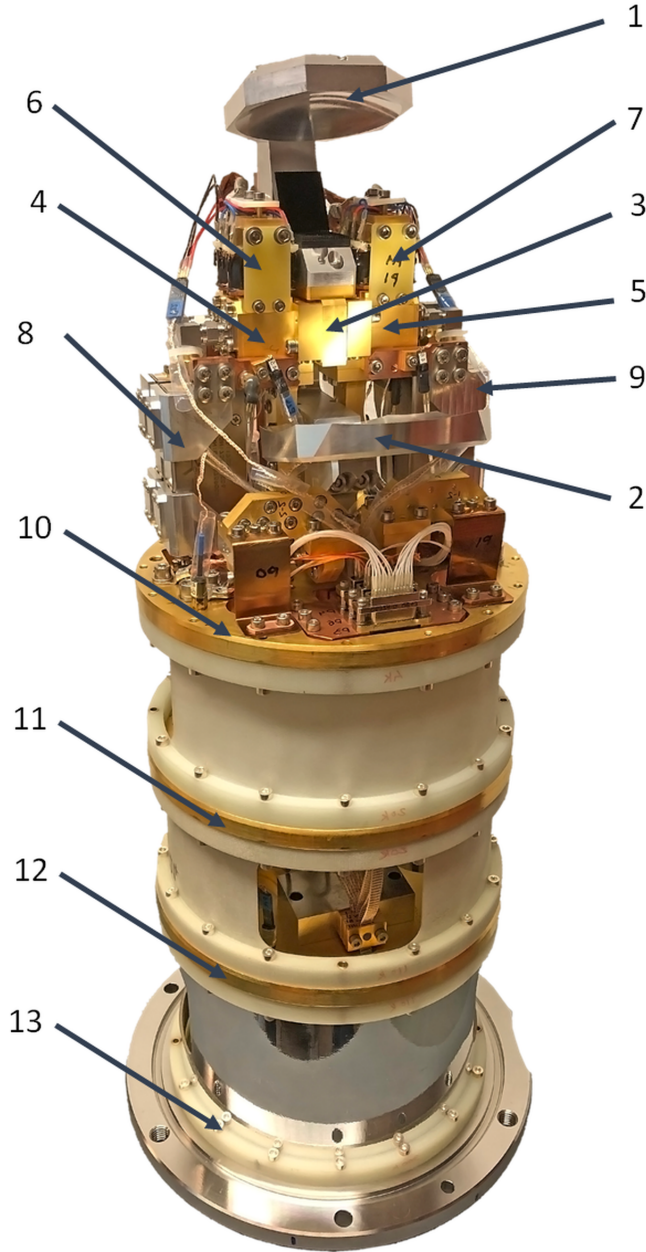
Fig. 2. SEPIA345 CCA layout. The following components are marked: 1 – the first cold mirror; 2 – the second cold mirror; 3 – the OMT; 4 – the 2SB mixer block at Pol0; 5 – the 2SB mixer block at Pol1; 6 – the magnetic coil assembly at Pol0; 7 – the magnetic coil assembly at Pol1; 8 – the LSB and USB IF assemblies at Pol0; 9 – the LSB and USB IF assemblies at Pol1; 10 – the 4K plate; 11 – the 15K plate; 12 – the 110 K plate; 13 – the room temperature plate.

Fig. 3. Mixer block details. (*a*) Photograph of the bottom part of the mixer block. The following components are marked: 1 – outputs from the LO power divider; 2 – LO directional couplers; 3 – the 90° RF hybrid; 4 – mixer circuits; 5 – the IF circuitry; 6 – the IF hybrid. (*b*). Detailed photograph of the mixer circuitry. The following components are marked: 1 – SIS junctions; 2 – the landing capacitor. The SIS mixer chip is placed in the mixer channels and is bonded to the IF extraction point through the landing capacitor, and to the ground at the choke structure.

instrument selecting mirror (position 2, Fig. 1) by several mirrors and through the RF signal window to the cold optics of the Cold Cartridge Assembly (CCA, position 6 in Fig. 1), which is compatible with ALMA receiver cartridges.

Details of the layout of the CCA are shown in Fig. 2. Two cold optics mirrors (positions 1 and 2 in Fig. 2, position 5 in Fig. 1) collimate the incoming signal further to a corrugated horn, followed by an orthomode transducer (OMT) that provides the polarization split (position 3, Fig. 2). Since both polarizations share the same feed horn, they are co-aligned on the sky. Lab measurement results confirmed a cross-polarization leakage lower than −25 dB over the entire operational band. The SEPIA
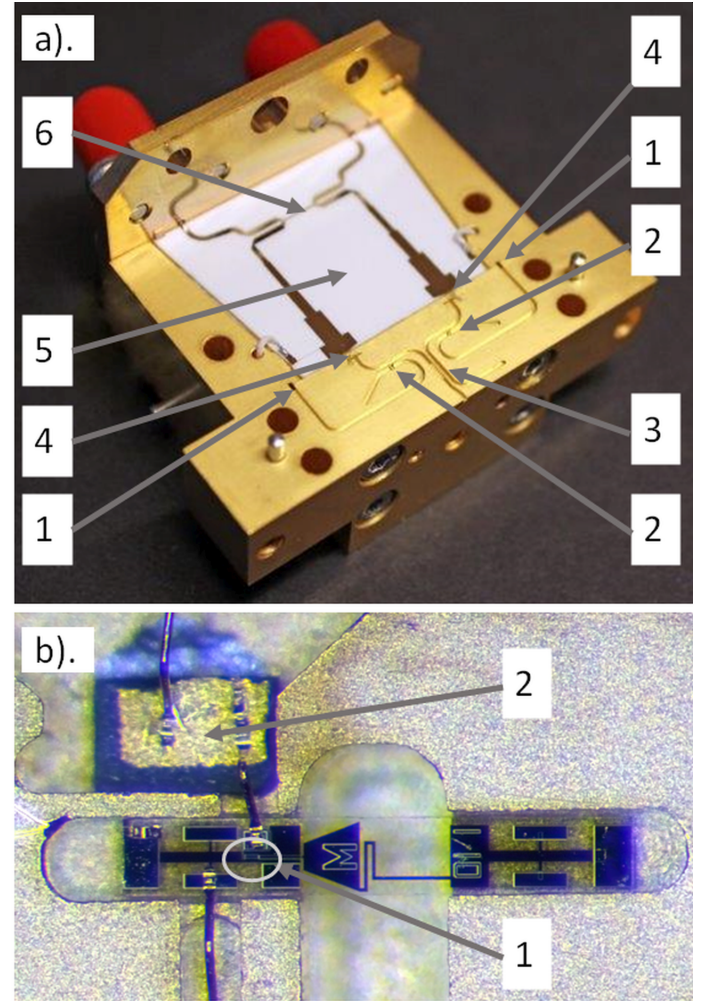
OMT is based on the ALMA Band 5 design (Belitsky et al. 2018b) but modified to cover the 271–377 GHz frequency range. The outputs of the OMT are situated on the opposite sides of the OMT unit. Used in combination with a compact 90° waveguide twist at one of the polarizations, namely polarization 1 (Pol1), the CCA layout allows the use of identical design 2SB mixer assemblies for both polarizations (positions 4 and 5, Fig. 2). The twist is adapted from a solution suggested by Rud et al. (2009), redesigned and optimized to enhance its fractional bandwidth, as well as for facilitating its fabrication. The resulting assembly is highly compact because of the small thickness of the twist (i.e., 0.4 mm).

Each of the 2SB mixer blocks (positions 4 and 5, Fig. 2) adopts a split-block design for the RF path and integrates a local oscillator (LO) path. The bottom part of the mixer block is shown in Fig. 3a. The LO path consists of a waveguide power divider, constructed on the other side of the mixer block, as well as an LO injection quadrature directional coupler. Outputs from the LO power divider are labeled as position 1 in Fig. 3a. The LO

directional couplers, one for each mixer element, provide about −18 dB coupling (position 2, Fig. 3a). Inside the mixer block, the RF path starts with a 90° hybrid, marked as position 3 in Fig. 3a. Mixer circuitry (position 4, Fig. 3a), and IF circuitry (position 5, Fig. 3a) including IF hybrid (position 6, Fig. 3a) with integrated broadband impedance transformers and bias-Ts are also located inside each of the two mixer blocks. The waveguide dimensions chosen for the receiver (e.g., $380\,\mu m \times 760\,\mu m$) place strict mechanical constrains on the fabrication accuracy of the receiver components. The RF hybrid offers phase and amplitude imbalances similar to the unit used in Meledin et al. (2019). The mixer chips (shown in Fig. 3b) circuitry relies on twin-junction $Nb/Al-Al_xO/Nb$ superconductor-isolator-superconductor (SIS) thin film technology (Pavolotsky et al. 2011), and contains two junctions with an area of $2.2-2.4\,\mu m^2$ (shown in Fig. 3b, position 1). The SIS junctions are connected in parallel and with a thin-film superconducting transmission line between them, to compensate the junctions' reactance at the signal frequency. This line is placed on 360 nm of SiO_2 sputtered on top of the RF choke, serving as a ground layer for the tuning circuitry. The mixer design resembles the SHFI Band2 (Risacher et al. 2006; Vassilev et al. 2008) mixer chip topology, but with the extraction of the signal at the IF from an additional port situated close to the SIS mixers and via a landing 0.9 pF capacitor (position 2, Fig. 3b) to ensure the flatness of the IF response across the 4–12 GHz band.

The IF outputs of the mixers are combined with the superconducting 90° 3 dB IF hybrid (position 6, Fig. 3a) via $15\,\Omega$ to $50\,\Omega$ impedance transformers with the built-in bias-Ts, all on the same alumina substrate. This integrated solution allows the IF assembly to take advantage of compact mixer biasing, optimal embedding IF impedance for the SIS junctions, and proper phasing of IF signals. The final separation of the signal to lower and upper sidebands (LSBs and USBs, correspondingly) occurs in the IF hybrid.

The IF hybrid is based on the design presented in Rashid et al. (2019), where all the lines are fabricated out of 5-μm-thick gold. In contrast, the actual IF hybrid features transmission lines, offering lower insertion losses with only 400-nm-thick Nb lines. However, this affected the coupling and required redesign and optimization of the component. The hybrid ensures excellent amplitude and phase imbalances with a typical value of less than 0.3 dB and 1°, correspondingly over the 4–12 GHz IF band (Rashid et al. 2019). Further amplification at IF is performed using low-noise cryogenic amplifiers (LNAs) preceded by 4–12 GHz isolators. As a result of all of the above design choices, 16 GHz (2×8 GHz) of instantaneous IF bandwidth is reached per polarization.

The LO covering 283–365 GHz was purchased from the National Radio Astronomy Observatory (NRAO). It is implemented with technology described in Bryerton et al. (2013). SEPIA345, as well as the other SEPIA receiver channels, uses a direct multiplication LO chain (the total multiplication factor for SEPIA345 is 18), following a Yttrium Iron Garnet (YIG) oscillator. The last frequency multipliers ($\times 3$) for each polarization are mounted inside the CCA at the 90 K stage (position 12, Fig. 2). Then the LO signal is delivered to the mixer blocks at the 4 K stage (position 10, Fig. 2), employing WR-10 waveguides with integrated waveguide size transitions. The YIG oscillator and other LO chain components are located in the Warm Cartridge Assembly (WCA), which is attached to the CCA and is also developed and built by NRAO. The WCA provides all the necessary interfaces for IF extraction, and bias for the receiver's components via a ALMA Front-End Bias Module (FEBM) and a

Control Unit (M&C). Finally, the WCA is completed with warm IF amplifiers, maintaining the IF signal levels for further IF signal processing. An external microwave synthesizer is used as a reference source for the phase-lock of the YIG during receiver operation.

2.3. SEPIA345 backend and receiver control

SEPIA345, as a part of the SEPIA instrument, interfaces to an IF processor and the FFTS (Klein et al. 2012), which are provided to APEX by MPIfR and together form the backend system. The IF processor is built in a modular way, and is located between the outputs of the SEPIA receivers and the FFTS. It provides pre-amplification and leveling of all analog IF receiver outputs, and then divides the 4–12 GHz input bandwidth for each sideband and polarization into two 4-GHz-wide bands, which are downconverted to the baseband (0–4 GHz) in a heterodyne mixing process. In summary, each IF module converts the 8 GHz input bandwidth into 2×4 GHz bands for the FFTS. The FFTS provides spectral resolution of up to 64k channels per 4 GHz of input bandwidth.

The SEPIA345 receiver channel is integrated into the SEPIA control system (Belitsky et al. 2018b). In order to perform all receiver related tasks during an astronomical observation, the communication with all SEPIA receiver components is carried out via the SEPIA control software, which listens to commands issued from the APEX observing control system (APECS; Muders 2021). The SEPIA control software also offers a graphical user interface (GUI), as well as a scripting interface, providing the desired flexibility for receiver health checks, characterization, tuning, and eventual troubleshooting. The complete band initialization process takes only a couple of minutes and consists of demagnetizing the coils (e.g., used to suppress the Josephson current), the defluxing of SIS mixers, stabilizing the mixer temperatures, setting default values of the magnetic coil currents, and setting the LNA parameters. During regular observations the tuning of the mixers is performed by APECS. In-band retuning, for instance, only changing the LO and setting optimal mixer bias values, takes less than 10 s. Moreover, switching between the three SEPIA receiver channels can be done within only a few minutes. The ability to quickly tune within a SEPIA band and to also switch between bands are important features of the SEPIA instrument, which allow valuable observation time to be saved.

3. Results of SEPIA345 commissioning

The technical verification of SEPIA345 took place after the installation of the band at APEX in February-March 2020. The science commissioning of the receiver band was then continuously performed until the middle of 2021, with this commissioning being carried out despite the impact of the COVID-19 pandemic on the APEX scientific and technical operations.

All ground-based observations at millimeter and submillimeter wavelengths are significantly affected by atmospheric transmission. Figure 4 shows atmospheric transmission at the Chajnantor plateau from 272 to 376 GHz for several values of precipitable water vapor (PWV): 0.2, 0.5, 1.0, 3.0, and 6.0 mm. The transmission curves have been calculated using the radiative transfer model from Pardo et al. (2001). The poor transmission at 325 GHz is due to strong absorption by the atmospheric water line. Also, the presence of atmospheric O_2 prevents good transmission near 368.5 GHz. Likewise, the atmospheric transmission at the highest frequencies is severely limited by the wing
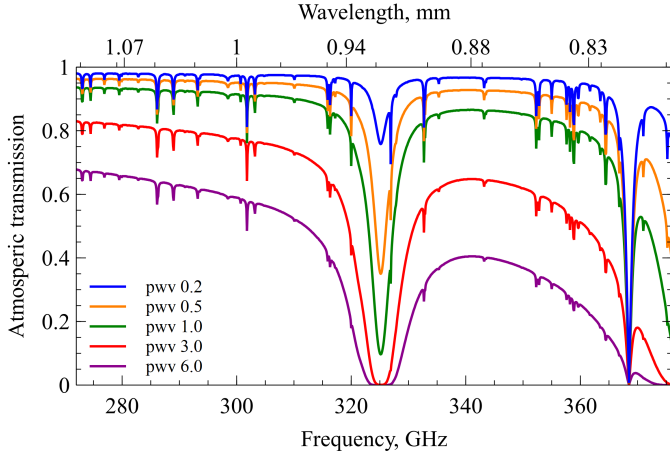
Fig. 4. Zenith atmospheric transmission at the Chajnantor plateau at different values of precipitable water vapor: i.e., 0.2, 0.5, 1.0, 3, and 6.0 mm in the frequency range covered by SEPIA345. The atmospheric transmission calculations are based on the ATM model from Pardo et al. (2001).

Table 1. Selection of important transitions in the SEPIA345 band.

Molecule	Transition	Frequency (GHz)
N_2H^+	$J = 3 \rightarrow 2$	279.51175
CS	$J = 6 \rightarrow 5$	293.912086
H_2O	$J_{K_a,K_c} = 10_{2,9} \rightarrow 9_{3,6}$	321.225677
H_2O	$J_{K_a,K_c} = 5_{1,5} \rightarrow 4_{2,2}$	325.152899
$C^{18}O$	$J = 3 \rightarrow 2$	329.330552
^{13}CO	$J = 3 \rightarrow 2$	330.587965
CO	$J = 3 \rightarrow 2$	345.795990
HCN	$J = 4 \rightarrow 3$	354.505478
HCO^+	$J = 4 \rightarrow 3$	356.734223
O_2	$N_J = 3_2 \rightarrow 1_1$	368.49825
H_2D^+	$J_{K_a,K_c} = 1_{1,0} \rightarrow 1_{1,1}$	372.42137

of the water line at 380 GHz. Typical weather conditions for using the receiver correspond to 0.5–1 mm of PWV.

In Table 1, some astrophysically important molecular transitions in the SEPIA345 frequency range are listed. Several of those lines were used during receiver commissioning (e.g., H_2O, CO). It is important to note that the 325 GHz water line needs to be red-shifted out of the atmospheric water line to be accessible even in good weather. Also, observations of lines around 368.5 GHz will be hampered due to the O_2 $N_J = 3_2 \rightarrow 1_1$ atmospheric line.

3.1. Noise temperature

Measurements of the receiver single sideband (SSB) noise temperature were performed with SEPIA345 mounted in APEX cabin A using the FCU and the telescope backend. The receiver noise temperatures were measured over the full RF band by tuning the LO in steps of 0.5 GHz. For each measurement a HOT Load–COLD Load–SKY calibration scan was taken and then a standard calibration was applied (Polehampton et al. 2019) to give a receiver noise temperature curve per sideband and polarization. Finally, the receiver noise temperature was averaged over each 4-GHz-wide FFTS section. Figure 5 illustrates the results of the measurements over the full band. The noise temperature
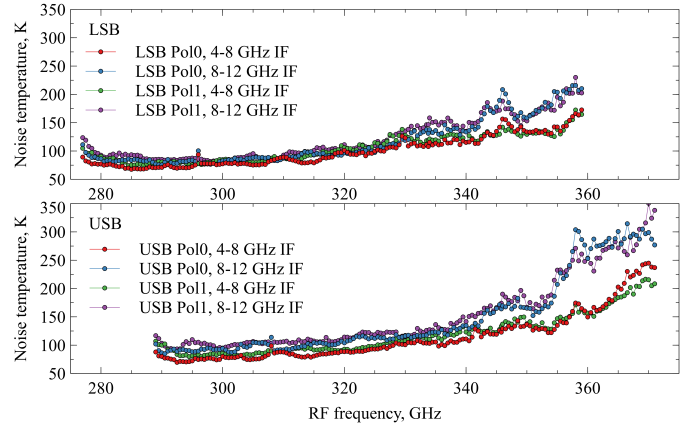

Fig. 5. SSB receiver noise temperature measurements performed for each polarization and sideband over the entire RF band averaged over each 4.0-GHz-wide FFTS IF sub-band. The temperature in the higher IF section (8–12 GHz) is illustrated with blue (Pol0) and violet circles (Pol1). The results in the inner segment (4–8 GHz) are shown with red (Pol0) and green circles (Pol1).
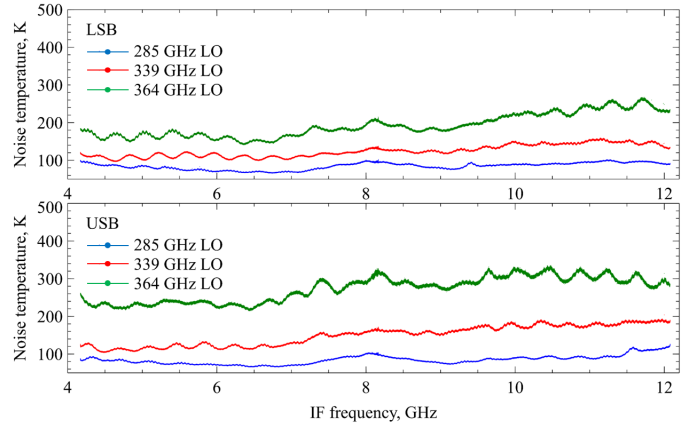

Fig. 6. SSB receiver noise temperature measurements as a function of IF performed for Pol0 and both sidebands at three LO frequencies: 285 GHz (blue curve), 339 GHz (red curve), and 364 GHz (green curve).

in the higher half of the IF band (8–12 GHz) is illustrated with blue circles for polarization 0 (Pol0) and violet circles for Pol1. Correspondingly, the results in the lower part of the IF band (4–8 GHz) are shown with red circles for Pol0 and green circles for Pol1.

As can be seen in Fig. 5, typical values of receiver temperature are $\lesssim$100 K below 320 GHz, approach 150 K at 340 GHz and then rise toward the high-frequency end of the receiver band. At the high side of the RF range, above 340 GHz, there is a noticeable difference in the noise temperature of the receiver averaged over the 4–8 GHz and the 8–12 GHz IF sub-bands. This is most likely associated with the deterioration of the mixers performance with dropped conversion gain, and the worse performance of some IF components, such as isolators and LNAs, at IF frequencies above 10 GHz increasing the noise contribution from these components. This conclusion is supported by the measurement results of the noise temperature for the Pol0 mixer as a function of the IF frequency, as performed at three different LO frequencies of 285 GHz, 339 GHz and 364 GHz, as shown in Fig. 6. The noise performance curves are nearly flat over the whole 4–12 GHz IF band at lower LO frequencies. However, toward the higher end of the RF band, a positive slope
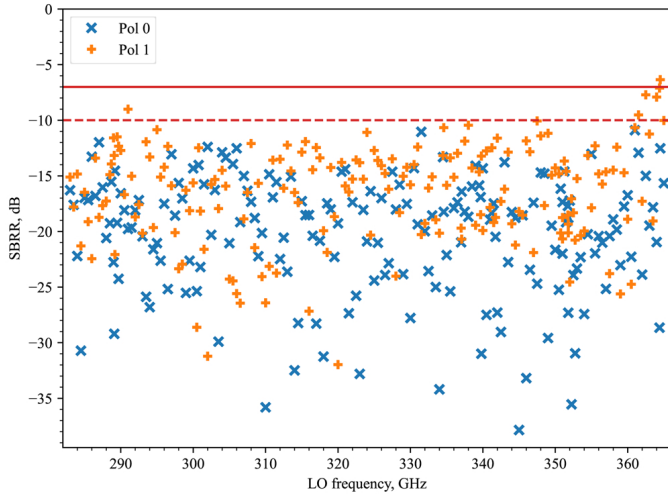
Fig. 7. Measured SBRR as a function of LO (at various positions within the 4–8 GHz part of the IF band). The solid and dotted red lines indicate −7 dB and −10 dB values of SBRR, respectively.
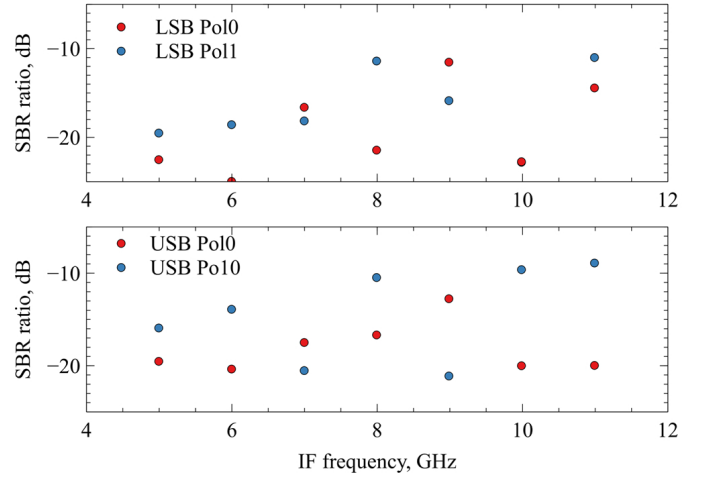

Fig. 8. Estimated SBRR over the 4–12 GHz IF at every 1 GHz, as determined by observations of the CO $J = 3 \rightarrow 2$ line toward WB 947 in the LSB (*top*) and in the USB (*bottom*).

of the noise temperature over the IF frequency becomes more pronounced. According to our investigation, the increase in the receiver noise temperature above 340 GHz could be caused by the interaction of the on-chip IF extraction circuitry and the SIS junction RF tuning circuitry.

3.2. Sideband rejection ratio

The sideband rejection ratio (SBRR) plays an important role for the ability to perform high-quality science observations, since these require as little contamination as possible in the signal band from lines in the image band. In the case of astronomical sources with high spectral line density (cf., Sgr B2, Nummelin et al. 1998), a poor SBRR will, for instance, severely hamper line identification.

The SBRR measurements obtained in the lab using the standard method (Kerr et al. 2001) prior to shipping the receiver to APEX showed the SBRR to be better than −10 dB over 80% of the band and about −7 dB at any frequency. To facilitate verification of the SEPIA345 receiver at the telescope at various LO tunings, a synthetic line emulator source was installed, directly illuminating the receiver window. The evaluation of SBRR is based on taking the ratio of measured IF line strength placed in the signal band to that of its appearance in the image band. This ratio is usually a good approximation of the SBRR when the gains are similar in the signal and image bands. As seen in Fig. 7, the overall average SBRR is as low as −18 dB. The Pol0 mixer demonstrates SBRR average values around −20 dB, while Pol1 channel average values lie around −15 dB, with a few values close to −7 dB toward frequencies above 360 GHz. Based on our analysis, at those high frequencies, the embedding impedance seen by the mixer could be quite different for the two mixers constituting the 2SB system. As a consequence, the amplitude and phase balances deviate, which results in the SBRR degradation.

Once APEX operations resumed in September 2020, after the COVID-related shutdown, SBRR measurements were also performed on-sky by observing a strong and narrow CO $J = 3 \rightarrow 2$ source, namely WB 947[2]. The CO line was placed at different parts of the IF band, by retuning the LO. For each LO setting,

the SBRR was evaluated by measuring the intensity ratio of the weakly appearing image line to the signal line. In Fig. 8, these estimates have been summarized, for placing the signal line in both the USB and the LSB. From Fig. 7, we can conclude that the SBRR values obtained from on-sky tests are in line with measurement results performed using the line simulator source. We also note that in the online APECS calibration software, only a single value of −15 dB is used for initial calibrations. However, one can recalibrate the data with other values of SBRR in the offline calibrator at particular frequencies of interest.

3.3. Stability

One of the most important receiver parameters is its stability. A standard method to characterize receiver stability is performing measurements of the Allan variance (Allan 1966; Schieder & Kramer 2001). For white (uncorrelated) noise, the variances of the receiver output power, σ^2, can be reduced by increasing the integration time, τ, as follows from the radiometer equation. When the noise spectrum contains additional correlated components, σ^2 starts to deviate from the equation after a certain integration time. Then this correlated noise (for instance, drift or 1/f noise) starts to dominate in the noise spectrum. The Allan time (τ_A) is the integration time corresponding to a minimum of Allan variance that is a crossover from white noise to 1/f or drift noise. For characterization, we consider both the total power and spectroscopic Allan variance. Those measurements were performed on various occasions at several sky frequencies, often at the frequency of transition CO $J = 3 \rightarrow 2$.

The measurements took place while the telescope was standing still (stowed). Because of the construction of the cabin, the warm load is located at the same height and just a couple of meters apart from the exhaust of the air conditioning system. The system maintains ambient temperature in the cabin at 13 ± 1 deg. Therefore, the cold load of the FCU provided more stable conditions than the cabin ambient temperature while data was being collected over several hours.

The total power Allan time was measured in small sub-bands combining consecutive FFTS channels, spanning a total bandwidth of 125 MHz per sub-band. Several of these sub-bands were sampled to compare the results over the IF band. In Fig. 9 we show the total power Allan variance that was obtained using the
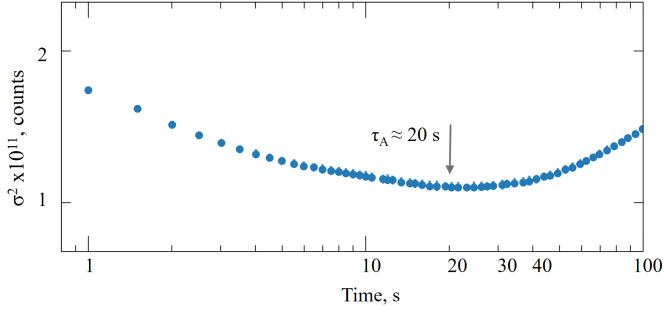
---

[2] See Wouterloot & Brand (1989), also known as LBN 1037.

Fig. 9. Example of total power Allan variance measurement performed for Pol0 LSB within a 125-MHz-wide sub-band in the 4–8 GHz FFTS segment at the LO frequency of 297 GHz.
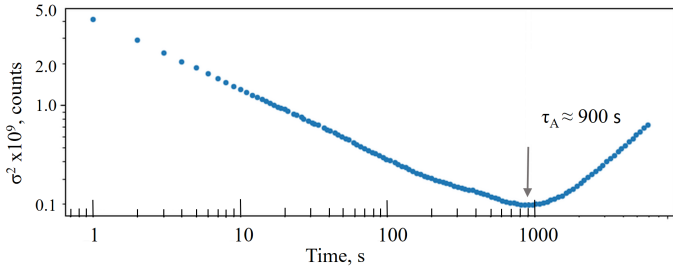

Fig. 10. Example of a spectroscopic power Allan variance measurements at a signal frequency of 345 GHz. The Allan variance time here is estimated to be better than 900 s. The FFTS response was recorded for more than 13 h.

Pol0 LSB within a 125-MHz-wide sub-band within the 4–8 GHz FFTS segment at the LO frequency of 297 GHz. This frequency is recommended for continuum observations as it is relatively free of atmospheric features. The IF power was recorded over 30 000 read-outs with a 0.5 s dump time. This corresponds to more than 4 h of measurements, which is more than adequate to determine Allan variance times longer than 20 s.

The spectroscopic Allan times are calculated by creating smaller sub-bands combining a few consecutive FFTS channels, spanning 1.0 MHz in total. Then, the signals of two of these 1.0 MHz sub-bands are subtracted, and their noise characteristics are studied. As previously stated, various combinations of 1.0 MHz sub-bands were analyzed to have a more complete overview of the behavior. An example of the spectroscopic Allan variance measurements is displayed in Fig. 10. These measurements were performed with Pol0 mixers at the 345 GHz LSB in the 4–8 GHz FFTS IF section using the difference between two different 1.0-MHz-wide sub-bands, some 700 MHz apart. The Allan time is estimated to be larger than 900 s.

Estimated values of the total power and spectroscopic Allan time are summarized in Table 2. The total power τ_A value is the average over several 125-MHz-wide sub-bands within the 4 GHz FFTS IF segment. The variation is indicated as a standard error.

3.4. Pointing accuracy, beam map, telescope efficiency, and observations at extreme frequencies

The absolute pointing accuracy of the SEPIA345 receiver is maintained by regular CO($J = 3 \rightarrow 2$) observations of carbon-rich circumstellar envelopes. The existing database of pointing sources, which is well-established, for example, by SEPIA's predecessor SHFI Band2 (Vassilev et al. 2008), consists of some 50 stars. In addition, continuum pointing scans on planets and

Table 2. SEPIA345 total power and spectroscopic Allan times (τ_A, in seconds) estimated at different signal frequencies.

Frequency (GHz), sideband	Spectroscopic τ_A (s) in 1 MHz	Total power τ_A (s) in 125 MHz	Notes
291, LSB	>150	18 ± 6	Used for cont. observ.
295, LSB	>80	16 ± 7	
321, USB	>60	20 ± 6	Near H$_2$O maser line
345, USB	>150	11 ± 4	CO $J = 3 \rightarrow 2$
356, USB	>70	13 ± 4	
371, USB	>90	11 ± 3	

Notes. The total power τ_A value is the average over several 125-MHz-wide sub-bands within the 4 GHz FFTS IF segment. The variation is indicated as a standard error.

some compact and bright HII regions are also used to obtain pointing corrections during science or technical observations. Several pointing runs have been conducted since the installation of the receiver channel. The sky offset rms scatter is about 3 arcsec. Focus offsets determined from planet scans are similar to the other SEPIA receivers. A typical pointing measurement is shown in Fig. 11.

In Fig. 12, a beam map created from observations of the water maser at 321 GHz toward VY CMa is displayed. This beam map consists of four on-the-fly (OTF) maps stacked together to improve the signal-to-noise ratio. The oxygen-rich star VY CMa is a well-known host of water masers (e.g., Menten & Melnick 1991). The 321 GHz water maser emission originates from energy levels near 2000 K in excitation energy and it can be considered as a point source with respect to the APEX beam size at 321 GHz. Map contours go up to 20% of peak integrated line intensity, thus showing the bottom part of the beam shape, including possible sidelobes. Given the noise level in the beam map, we can only state that the sidelobe level is less than 4%. As can be seen in Fig. 12, a Gaussian full half-power beam width (HPBW) of 18.2 arcsec is fitted. The beam shape is nearly Gaussian but slightly more flat-topped. As noted above, SEPIA345 optics implementation aims at an edge taper of –12 dB (Lapkin et al. 2019). This value of edge taper corresponds to a calculated full HPBW of 18.6 arcsec assuming a quadratic distribution of the illumination over the subreflector (Baars 2007). If a Gaussian is fitted to this near-Gaussian beam shape, we arrive at a full HPBW of 18.0 arcsec. This is very near the 18.2 arcsec value we get from our beam map. Taking into account a typical error of about 5% for the beam maps, we recommend using full HPBW of 18.7 ± 0.5 arcsec for the beam shape, including effects of the near –12 dB tapering and for observations at 321 GHz.

The telescope efficiency was determined from observations of planets using the antenna temperature peak values obtained near the center of the cross scans (using both wobbler switching or position switching) in azimuth and elevation. Also, continuum observations of planets and compact HII regions are preferably performed at 291 GHz since the atmospheric transmission is often high (see Fig. 4) and no strong molecular transitions occur around this frequency. Mars has a varying and noncentric brightness distribution over its surface[3] as seen from Earth, which may have to be taken into account if resolved. The planet brightness temperatures were obtained from the Gildas ASTRO
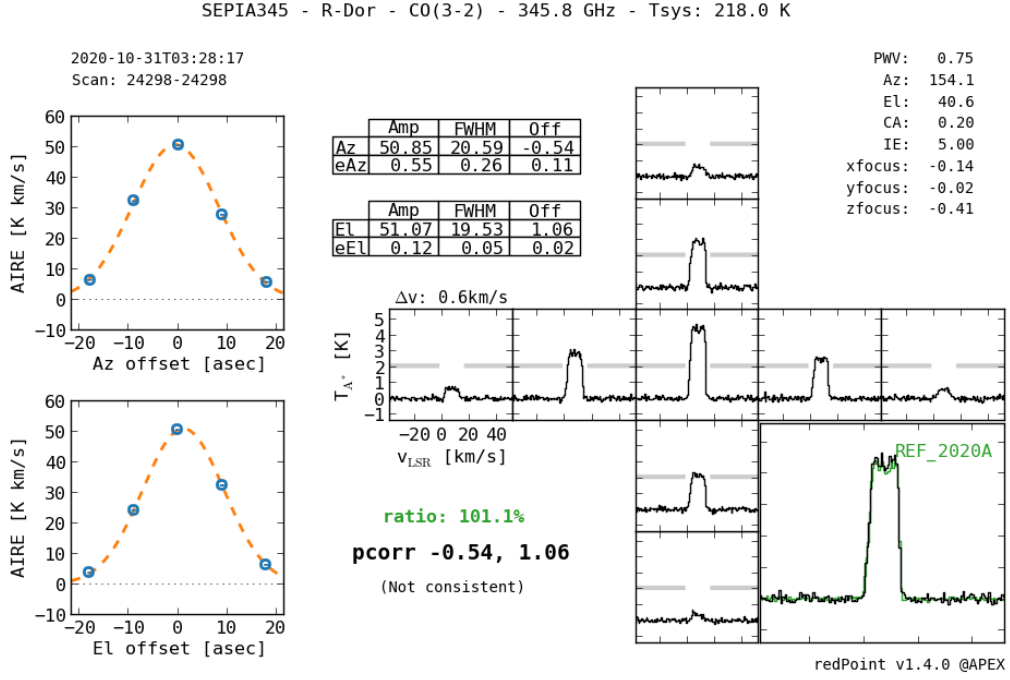
---

[3] https://lesia.obspm.fr/perso/emmanuel-lellouch/mars/index.php

SEPIA345 - R-Dor - CO(3-2) - 345.8 GHz - Tsys: 218.0 K

Fig. 11. Example pointing measurement toward the circumstellar envelope of R Dor using the CO($J = 3 \rightarrow 2$) line.
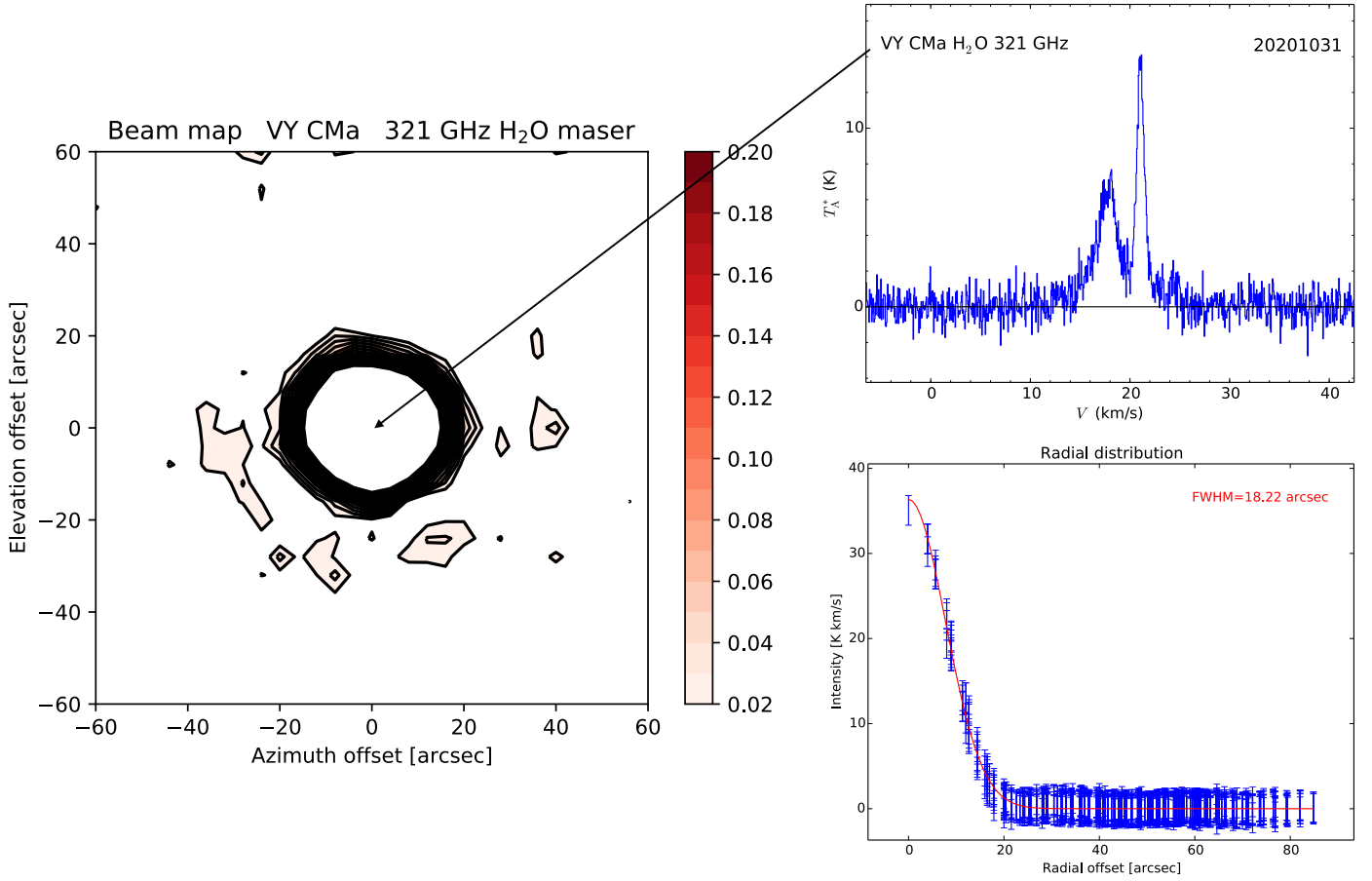

Fig. 12. Beam map toward the circumstellar envelope around VY CMa using the 321 GHz water maser line. Map contours start at 2% of the peak integrated intensity and are shown up to 20% in steps of 1%. The spectrum at the map center position is shown, as well as the radial distribution in terms of line integrated intensity.
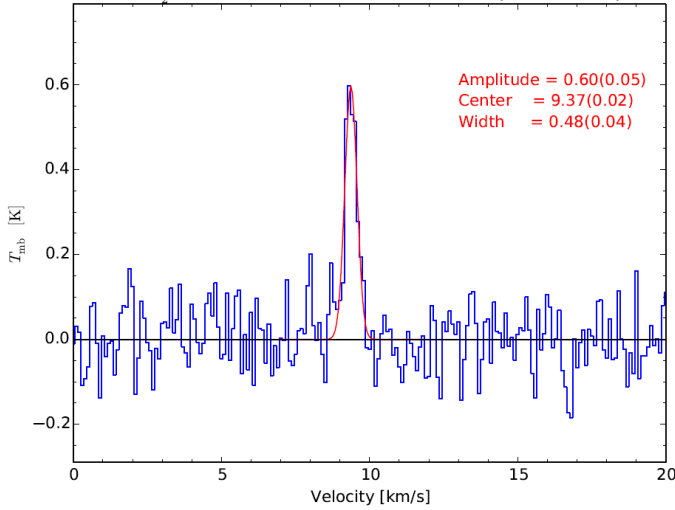
Fig. 13. H_2D^+ line detection toward the prestellar core SMM6 in the Ori-B9 region at 372 GHz. The vertical scale is in T_{mb} and the velocity scale is with respect to local standard of rest. The derived line center (km s^{-1}), line width (km s^{-1}), and peak intensity obtained from a Gaussian fit (in red) are included.

package[4] or from Butler (2012). As a result, the recommended values of the efficiencies at 291 GHz (in October-December, 2020, when the antenna surface rms was about 13 μm) are the following: the beam efficiency, η_{mb}, is 0.72 ± 0.05; the aperture efficiency, η_a, is 0.63 ± 0.05; and the ratio of the flux to observed source antenna temperature corrected for atmospheric attenuation, radiative loss, scattering, and spillover, S/T_A^*, is 38 ± 3 Jy K^{-1}. The overall calibration uncertainty is estimated to be around 10%. This is estimated from the uncertainties of the individual parameters such as beam size, adopted planet brightness, and noise in the observed intensity. In order to follow up on these parameters and track their evolution in time, regular planet observations form a part of the SEPIA calibration plan.

In addition to carrying out extensive calibration observations of SEPIA345 at 321 GHz near the center of its observing band, the receiver has also been tested at its extreme operating frequencies. As an example, Fig. 13 shows H_2D^+ line observations of the prestellar core SMM6 in the Ori B9 region at 372 GHz . The velocity resolution is 0.2 km s^{-1} with channel noise of 73 mK (in about 1 h of integration time) and the vertical axis represents the main beam temperature, T_{mb}. The Pol1 data were recalibrated with the actual SBRR value before averaging with the Pol0 data. The result is in line with the observations by Miettinen (2020).

4. Conclusion

The SEPIA345 receiver channel, installed at the APEX telescope in February 2020, covers a signal band of 272–376 GHz. The dual polarization receiver employs 2SB SIS mixers and provides an instantaneous IF bandwidth of 4×8 GHz. The receiver temperature values are typically below 100 K at frequencies lower than 320 GHz, approach 150 K at 340 GHz, and increase toward the high-frequency end of the band. The receiver has an average

SBRR of –20 dB and –15 dB measured at the telescope for the Pol0 and Pol1 mixer channels, respectively. The receiver stability measurements demonstrate typical total power Allan times on average larger than 10 s in the 125 MHz effective noise bandwidth and better than 60 s spectroscopic Allan times in the 1 MHz effective noise bandwidth.

The SEPIA345 receiver became part of the suite of APEX facility instruments after its successful commissioning in July 2021. The receiver is now available to all APEX observers. By the end of 2021, about 170 h of science observations had been conducted.

References

Akiyama, K., Alberdi, A., Alef, W., et al. 2022, ApJ, 930, L12
Allan, D. W. 1966, IEEE Proc., 54, 221
Baars, J. W. M. 2007, The Paraboloidal Reflector Antenna in Radio Astronomy and Communication, 348
Baryshev, A. M., Hesper, R., Mena, F. P., et al. 2015, A&A, 577, A129
Belitsky, V., Bylund, M., Desmaris, V., et al. 2018a, A&A, 611, A98
Belitsky, V., Lapkin, I., Fredrixon, M., et al. 2018b, A&A, 612, A23
Bryerton, E., Saini, K., Muehlberg, J., Vaselaar, D., & Thacker, D. 2013, in IEEE MTT-S International Microwave Symposium Digest, 6697622
Butler, B. 2012, in ALMA Memo 594 Flux Density Models for Solar System Bodies in CASA
Event Horizon Telescope Collaboration (Akiyama, K., et al.) 2019, ApJ, 875, L1
Güsten, R., Nyman, L. Å., Schilke, P., et al. 2006, A&A, 454, L13
Hacar, A., Tafalla, M., Kauffmann, J., & Kovács, A. 2013, A&A, 554, A55
Hacar, A., Hogerheijde, M. R., Harsono, D., et al. 2020, A&A, 644, A133
Kerr, A., Pan, S.-K., & Effland, J. E. 2001, in ALMA Memo 357 Sideband Calibration of Millimeter-Wave Receivers
Khudchenko, A., Hesper, R., Baryshev, A. M., Barkhof, J., & Mena, F. P. 2017, IEEE Trans. Terahertz Sci. Technol., 7, 2
Klein, B. 2020, in Ringberg-Workshop APEX 2020
Klein, B., Hochgürtel, S., Krämer, I., et al. 2012, A&A, 542, A3
Lapkin, I., Ferm, S.-E., Fredrixon, M., et al. 2019, in Thirtieth International Symposium on Space Terahertz Technology, 150
Meledin, D., Pavolotsky, A., Desmaris, V., et al. 2009, IEEE Trans. Microwave Theory Tech., 57, 89
Meledin, D., Desmaris, V., Sundin, E., et al. 2019, in Thirtieth International Symposium on Space Terahertz Technology, 164
Menten, K. M., & Melnick, G. J. 1991, ApJ, 377, 647
Miettinen, O. 2020, A&A, 634, A115
Muders, D. 2021, Tech. Rep. APEX-MPI-MAN-0011
Nummelin, A., Bergman, P., Hjalmarson, Å., et al. 1998, ApJS, 117, 427
Pardo, J. R., Cernicharo, J., & Serabyn, E. 2001, IEEE Trans. Antennas Propag., 49, 1683
Pavolotsky, A. B., Dochev, D., & Belitsky, V. 2011, J. Appl. Phys., 109, 024502
Polehampton, E., Hafok, H., & Muders, D. 2019, Tech. Rep. APEX-MPI-MAN-0012
Rashid, H., Meledin, D., Desmaris, V., Sundin, E., & Belitsky, V. 2019, in Thirtieth International Symposium on Space Terahertz Technology, 50
Revéret, V., André, P., Le Pennec, J., et al. 2014, SPIE Conf. Ser., 9153, 915305
Risacher, C., Vassilev, V., Monje, R., et al. 2006, A&A, 454, L17
Rud, L., Kulik, D., & Kirilenko, A. 2009, Microwave Opt. Technol. Lett., 51, 851
Schieder, R., & Kramer, C. 2001, A&A, 373, 746
Siringo, G., Kreysa, E., Kovács, A., et al. 2009, A&A, 497, 945
The CONCERTO Collaboration (Ade, P., et al.) 2020, A&A, 642, A60
Vassilev, V., Meledin, D., Lapkin, I., et al. 2008, A&A, 490, 1157
Wiedner, M. C., Wieching, G., Bielau, F., et al. 2006, A&A, 454, L33
Wouterloot, J. G. A., & Brand, J. 1989, A&AS, 80, 149